

6D-ViT: Category-Level 6D Object Pose Estimation via Transformer-based Instance Representation Learning

Lu Zou, Zhangjin Huang

Abstract—This paper presents 6D-ViT, a transformer-based instance representation learning network, which is suitable for highly accurate category-level object pose estimation on RGB-D images. Specifically, a novel two-stream encoder-decoder framework is dedicated to exploring complex and powerful instance representations from RGB images, point clouds and categorical shape priors. For this purpose, the whole framework consists of two main branches, named Pixelformer and Pointformer. The Pixelformer contains a pyramid transformer encoder with an all-MLP decoder to extract pixelwise appearance representations from RGB images, while the Pointformer relies on a cascaded transformer encoder and an all-MLP decoder to acquire the pointwise geometric characteristics from point clouds. Then, dense instance representations (*i.e.*, correspondence matrix, deformation field) are obtained from a multi-source aggregation network with shape priors, appearance and geometric information as input. Finally, the instance 6D pose is computed by leveraging the correspondence among dense representations, shape priors, and the instance point clouds. Extensive experiments on both synthetic and real-world datasets demonstrate that the proposed 3D instance representation learning framework achieves state-of-the-art performance on both datasets, and significantly outperforms all existing methods.

Index Terms—6D object pose estimation, 3D object detection, vision transformer, representation learning.

I. INTRODUCTION

OBJECT pose estimation refers to predicting the location and orientation of 3D objects, which is a fundamental problem in robotic applications, such as grasping and manipulation. In recent years, remarkable progress [1]–[12] has been made for instance-level 6D object pose estimation, where exact 3D CAD models and their sizes are available in advance. Unfortunately, considering the diversity of object instances as well as the cost for building a CAD model for each instance, these methods are difficult to generalize to real practice.

Recently, category-level 6D object pose estimation has begun to receive more and more attention [13]–[18] given its practical importance. Compared with the instance-level problem, the goal of this task is to predict the 6D pose of unseen object instance of the same category for which no CAD model is available. In general, the classical instance-level pose estimation methods usually predict the object pose by establishing the correspondence between the RGB or RGB-D image and its CAD model. However, in the category

Lu Zou and Zhangjin Huang are with University of Science and Technology of China, Hefei 230031, China (e-mail: lzou@mail.ustc.edu.cn; zhuang@ustc.edu.cn).

Manuscript received April 19, 2005; revised August 26, 2015.

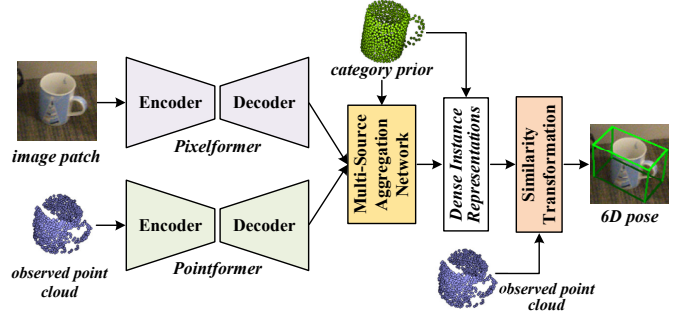


Fig. 1. The main network of our transformer-based instance representation learning network for category-level 6D object pose estimation.

level scenario, since there is no specific CAD model, it is quite difficult to directly establish this correspondence. In addition, even within the same category, objects could exhibit significant variations in shape, color, and size. Consequently, due to the large intra-class variations in texture and shape among instances, category-level pose estimation is much more challenging than instance-level problem [19].

In order to achieve reliable category-level object pose estimation, Wang *et al.* [18] innovatively proposed Normalized Object Coordinate Space (NOCS) as a shared canonical representation of all object instances within a category. Since the CAD model of the object is unknown, they reconstruct the canonical model representation in the NOCS space, and establish the dense correspondence between the reconstructed NOCS model with instance images or point clouds to realize 6D pose estimation. Later on, Tian *et al.* [17] improved the NOCS model reconstruction process by introducing shape priors. They extract category features from the shape priors as auxiliary information of instance features, so as to alleviating the shape variations across instances within the same category. Recently, Chen *et al.* [15] proposed FS-Net to further improve the quality of category-level pose features. They employ a shape-based 3D graph convolution autoencoder to extract the latent feature through the observed points reconstruction, and a decoupled rotation mechanism is proposed to decode instance rotation information from the latent feature. Despite the promising performance gains, this method is too complex, and it requires training separate models for different object categories due to their specific data augmentation.

In this work, we tackle the problem of category-level object pose estimation from the perspective of unified and powerful instance representation learning on RGB-D data.

More specifically, inspired by the most famous transformer architectures [20]–[24] that are widely concerned by natural language processing and computer vision communities, we have developed a two-stream transformer-based encoder-decoder architecture: 6D-ViT, for highly accurate category-level object pose estimation. To the best of our knowledge, this is the first attempt to apply vision transformers to the object pose estimation problem. Our network is composed of a Pixelformer and a Pointformer, which are used to explore the appearance and geometric characteristics of the object instance, respectively. Then, the dense representations (*i.e.*, correspondence matrix, deformation field) of the object instance are obtained through the fusion of the appearance information, and geometric information from different sources. Finally, the category-level 6D pose is obtained by establishing the correspondence among dense representations, categorical shape priors, and the observed point clouds. The comprehensive experiments on both synthetic (CAMERA25) and real-world (REAL275) datasets suggest that the proposed method has gained substantial performance improvements on both datasets, and achieved state-of-the-art performance through a unified model for all categories.

Our contributions can be summarized as follows.

- We present a novel two-stream category-level 6D object pose estimation network based on the transformer architectures. The network can semantically enhance the quality of instance representations by capturing long-range contextual dependencies of elements from RGB images and point clouds, respectively.
- Our network includes a Pixelformer and a Pointformer, both of which are encoder-decoder architectures for efficient dense instance representation learning.
- Extensive experiments demonstrate that our proposed 6D-ViT achieves state-of-the-art performance on both the CAMERA25 and REAL275 datasets, and significantly outperforms existing works.

The remainder of this paper is organized as follows. Section II briefly reviews some related works about 6D object pose estimation including instance-level (Section II-A) and category-level (Section II-B). Section III introduces the presented method in detail, which is composed of the overall framework (Section III-A), instance representation learning on RGB images (Section III-B), instance representation learning on point clouds (Section III-C), joint and dense representation generation and pose estimation (Section III-D) and loss functions (Section III-E). The experimental results of our network with comparisons to existing methods are reported in Section IV. Specifically, we evaluate the proposed method in terms of 6D object pose estimation (Section IV-D), and 3D model reconstruction (Section IV-E). In addition, the ablation studies of our network are discussed in Section IV-F. Finally, conclusions and future directions are provided in Section V.

II. RELATED WORK

A. Instance-Level 6D Object Pose Estimation

A large amount of research has focused on instance-level object pose estimation, in this section, we will only discuss

some of the most notable studies. According to the format of the input data, instance-level pose estimation methods can be broadly divided into RGB-based and RGB-D-based. Traditional RGB-based methods [1], [25] realize pose estimation by detecting and matching keypoints with the known 3D CAD model of the object. However, these methods rely heavily on hand-crafted features, which are not robust to low-texture objects and cluttered environments. Recently, many works apply deep learning techniques to this task due to its robustness to environment variations. Kehl *et al.* [3] extended the 2D object detection network [26] to predict the identity of the object, the 2D bounding box and the discretized orientation. Tekin *et al.* [9] proposed to firstly detect the keypoints of the object, and then solve a Perspective-n-Point problem for pose estimation. Zakharov *et al.* [12] estimated the dense 2D-3D correspondence map between the input image and the object model. Peng *et al.* [7] presented to predict a unit vector at each pixel pointing towards the keypoints. Song *et al.* [27] improved [7] by utilizing keypoints, edge vectors, and symmetry correspondence to express different geometric information in the input image.

As more and more RGB-D datasets are available, another line of work [2], [5], [10] began to apply both RGB and depth images to improve the pose estimation accuracy. Considering the different distributions of RGB and depth data, there are several different ways to deal with these two modalities. Kehl *et al.* [2] simply concatenate RGB and depth values, and feed the 4-channel data into a multi-stage model to produce pose estimations. Xiang *et al.* [11] firstly predict a rough 6D pose from the RGB image, followed by Iterative Closest Point (ICP) algorithm [28] using depth image for refinement. Wang *et al.* [10] proposed DenseFusion, they designed a two-branch framework to exploit the features of RGB and depth images separately, and fuse the features of different modalities through a Fully Connected (FC) layer. DenseFusion achieves state-of-the-art performance while reaching almost real-time inference speed. Nevertheless, it merges the features of two modalities in a straightforward manner, which is not sufficient to capture their inherent correlations. To this end, Zou *et al.* [29] further improved the feature fusion process in DenseFusion [10], they developed a cross-modality attention scheme to learn the feature interactions between the RGB images and point clouds. Our approach also estimates 6D object pose from RGB-D images, by contrast, we focus on a more general setting where the object CAD models are not available during inference.

B. Category-Level 6D Object Pose Estimation

There are only a few previous works [13]–[18] focus on estimating the 6D pose of unseen objects. Compared to instance-level problem, the category-level task is much more challenging due to the large intra-class variations in aspects of texture and shape among instances. To handle the above issue, some researchers proposed to construct an intermediate instance representation to mitigate such difference. Wang *et al.* [18] presented to represent different object instances within a category as a shared Normalized Object Coordinate Space (NOCS). They train a region-based deep network to infer

the correspondence from observed pixels to points in NOCS. As a result, the 6D pose and size can be calculated by shape matching between the predicted correspondence and the observed points. Chen *et al.* [14] introduced a unified category representation for a large variety of instances called canonical shape space (CASS). Additionally, a variational auto-encoder (VAE) is trained to estimate the category-level object pose. Similar to [14], Tian *et al.* [17] proposed SPD, which leverages the category-sensitive features to explicitly model the shape variation when reconstructing the NOCS model. Specifically, they enhanced the RGB-D features through introducing shape priors as an aid to the process of NOCS model reconstruction. In order to explore better pose-related features, Chen *et al.* [15] proposed FS-Net, it first extracts the latent instance features through the observed points reconstruction with a shape-based 3D graph convolution autoencoder. Then, a decoupled rotation mechanism was proposed to decode instance rotation information from the instance features. In order to increase the generalization ability of the network, an online 3D deformation mechanism is also proposed for data augmentation. Despite the impressive performance gains, this method is too complex, and it requires training separate models for different object categories due to their specific data preprocessing, which is not convenient for practical use. More recently, Lin *et al.* [16] presented DualPoseNet to learn rotation-equivariant shape features, it stacks two parallel pose decoders at the top of a shared pose encoder, where the implicit decoder predicts object poses with a working mechanism different from that of the explicit one. Thus to impose complementary supervision on the training of pose encoder.

Our work is based on SPD [17], and gets inspiration from the latest transformer architectures [20]–[24] which are successfully applied in natural language processing and computer vision. Specifically, we design two transformer-based encoder-decoder networks to individually explore the compact instance representations from the RGB images and point clouds. The experimental results demonstrate that our method achieves state-of-the-art performance and significantly outperforms existing works.

III. METHOD

Given a calibrated RGB-D image pair, our goal is to predict the 6D object pose represented by a rigid transformation $[R|t]$, where $R \in SO(3)$ and $t \in \mathbb{R}^3$. In order to handle scenes containing multiple instances, we first apply an off-the-shelf instance segmentation network (*i.e.*, Mask R-CNN [30]) to detect and segment objects in the scene. Next, the yielded object bounding box is exploited to crop the RGB image into image patches, and the segmentation mask is leveraged to convert the depth image into observed point clouds according to the camera intrinsic parameters. After that, image patches, observed point clouds, and categorical shape priors are fed into the main part of our network.

A. Architecture Overview

As shown in Fig. I, our main network consists of three subnetworks: (1) Pixelformer for instance representation learning

on RGB images (Section III-B); (2) Pointformer for instance representation learning on point clouds (Section III-C); (3) multi-source aggregation (MSA) network for joint and dense representation generation and pose estimation (Section III-D). More specifically, the image patches \mathcal{I} , and observed point clouds \mathcal{P} are firstly passed through the Pixelformer and Pointformer to learn instance representations existing in different modalities respectively. Then, the instance representations in the two modalities, denoted as F and \mathcal{F} , will be fused and enhanced by the category-sensitive representations extracted from the categorical shape priors \mathcal{P}_{pri} to generate the joint and dense instance representations (*i.e.*, correspondence matrix \mathcal{A} , deformation field \mathcal{D}_{def}). Finally, the dense representations, categorical shape priors and observed instance point clouds are leveraged by the Umeyama algorithm [31] to calculate the 6D object pose $[R|t]$. In addition, the loss functions used to train the whole network are introduced in Section III-E. The design details about each step are discussed below.

B. Instance Representation Learning on RGB Images

As depicted in Fig. 2, the Pixelformer is an encoder-decoder architecture which consists of two main components: 1) a multi-scale transformer encoder which contains I stages to generate high-resolution coarse appearance embeddings and low-resolution fine appearance embeddings; and 2) an MLP decoder to up-sample and aggregate the pyramid features to produce the pixelwise instance appearance representations.

1) *Multi-Scale Transformer Encoder*: The design of the transformer encoder in our Pixelformer is partly inspired by the latest multi-scale vision transformer: PVT [22], and is tailored and optimized for our task. Specifically, our multi-scale transformer encoder consists of four stages with different latent feature dimensions. In each stage i , it has an overlapped patch embedding (OPE) layer and two layers of alternating spatial reduction based multi-head attention (SRMA) and convolutional feed-forward network (C-FFN). Besides, we employ InstanceNorm (IN) before each SRMA and C-FFN module, and also provide residual connections around each of them.

a) *Overlapped Patch Embedding*: In vision transformers, patch embedding is usually used to combine non-overlapping image or feature patches. However, since the patches are non-overlapping, it fails to preserve the local continuity around those patches. In this work, we utilize overlapped patch embedding as introduced in [23] to tokenize images. Specifically, given an input RGB image with resolution of $H \times W \times 3$, we define K as the patch window size, S as the stride between two adjacent patches, and P as the padding size, we first split the input image into $\frac{H}{2^{(i+1)}} \times \frac{W}{2^{(i+1)}}$ patches and each patch with size of $K_i \times K_i \times C_{i-1}$, where $i \in \{1, 2, 3, 4\}$ and $C_0 = 3$. Then, the patch embedding process performs patch merging via linear projection on these patches to produce feature maps with the same dimensions as the non-overlapping process. In the experiments, we set $K_1 = 7$, $S_1 = 4$, $P_1 = 3$, and $K_j = 3$, $S_j = 2$, $P_j = 1$ where $j \in \{2, 3, 4\}$. As a result, we can obtain the multi-scale features $\{F_i | i = 1, 2, 3, 4\}$ with the shape of $\{\frac{H}{4} \times \frac{W}{4} \times C_1, \frac{H}{8} \times \frac{W}{8} \times C_2, \frac{H}{16} \times \frac{W}{16} \times C_3, \frac{H}{32} \times \frac{W}{32} \times C_4\}$. Following the design rules of ResNet [32], we use small output channels in shallow stages, *i.e.*, $C_i > C_{i-1}$ for $i \in \{1, 2, 3, 4\}$.

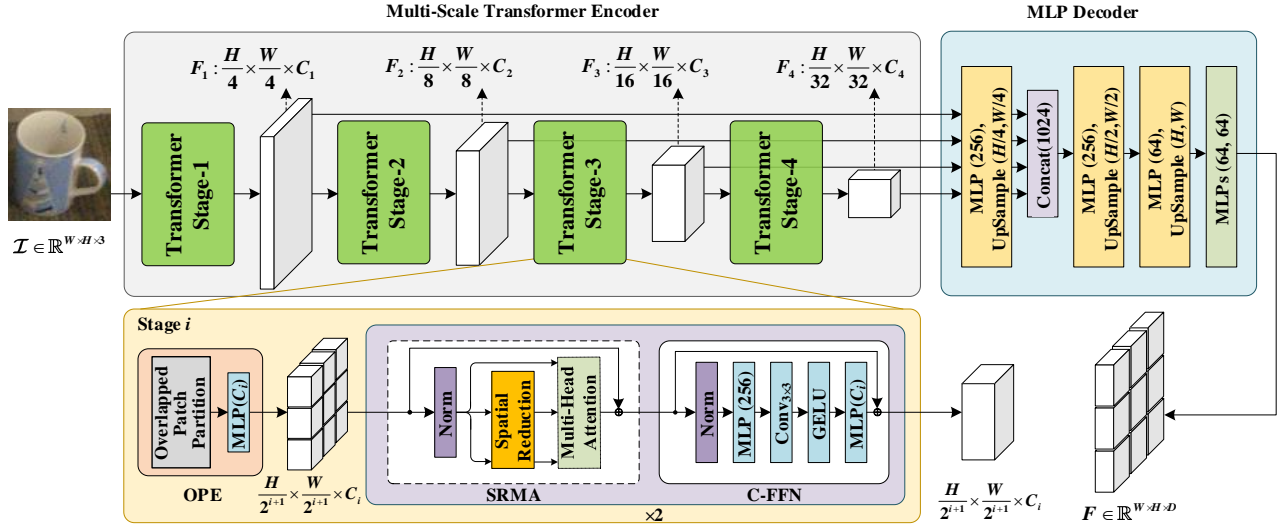


Fig. 2. The structure of the proposed Pixelformer. The network consists of two main modules: a multi-scale transformer encoder to extract coarse and fine appearance embeddings from RGB images; and an MLP decoder to fuse the multi-scale embeddings and generate the pixelwise object appearance representations. Note that in the figure, each item in the format of $Function(\cdot, \dots, \cdot)$ denotes the feature dimension after the corresponding operation.

b) *Spatial Reduction based Multi-Head Attention*: Considering the original multi-head attention mechanism [21], given a series of vectors $Q_i, K_i, V_i = \text{MLP}(C_i, C_i)(F_i)$, $i \in \{1, 2, 3, 4\}$ at each stage i , where each head of Q_i, K_i, V_i has the same shape of $(\frac{H}{2^{(i+1)}} \times \frac{W}{2^{(i+1)}}) \times d_{\text{head}(i)} = (H_i \cdot W_i) \times d_{\text{head}(i)}$. Here, $\mathcal{N} = (H_i \cdot W_i)$ is the length of a sequence, $d_{\text{head}(i)}$ refers to the dimension of each head at each stage, which is computed as $d_{\text{head}(i)} = C_i/M_i$, with M_i as the number of attention heads. Note that in the format of $Function(b, c)(a)$ in the full text, a represents the input feature vector, b and c represent the dimensions of the input and out feature, respectively. Therefore, the multi-head attention operation is calculated as:

$$\text{Attention}(Q_i, K_i, V_i) = \text{Softmax}\left(\frac{Q_i K_i^T}{\sqrt{d_{\text{head}(i)}}}\right) V_i, \forall i. \quad (1)$$

The computational complexity of Eq. (1) is $O(\mathcal{N}^2)$, which is prohibitive for large feature resolutions. Instead, we utilize the reduction process introduced in PVT [22] which uses a reduction ratio R_i in stage i to reduce the spatial scale of K and V before the attention operation executes. The spatial reduction (SR) operation is defined as follows:

$$\text{SR}(x) = \text{Reshape}(\text{IN}(x), R_i) \mathcal{W}_i, x \in \{K_i, V_i\}, \forall i. \quad (2)$$

In Eq. (2), $\text{Reshape}(x, R_i)$ is the operation of reshaping the input $x \in \mathbb{R}^{\mathcal{N} \times C_i}$ to the sequence with the shape of $\frac{\mathcal{N}}{R_i^2} \times (R_i^2 \cdot C_i)$, and $\mathcal{W}_i \in \mathbb{R}^{(R_i^2 \cdot C_i) \times C_i}$ refers to a linear projection operation that reduces the dimension of the input x to C_i . Hence, the complexity of the self-attention mechanism is reduced from $O(\mathcal{N}^2)$ to $O(\mathcal{N}^2)/R$. In the experiments, we set R^2 to $[64, 16, 4, 1]$ from stage one to stage four. Without abuse of notation, we denote the multi-scale features after SRMA as $\{F_i | i = 1, 2, 3, 4\}$ which is the same as the input.

c) *Convolutional Feed-Forward Network*: Previous transformer-based image encoders only employed MLPs as their feed-forward network (FFN), and completely relied on the self-attention mechanism to achieve feature enhancement. Although effective, this design cannot perceive the locality and translation-invariance of the object, and ignores the inter-pixel dependencies that play a critical role in object pose estimation. Based on this, we propose to insert convolutional operations into the FFN.

Specifically, we insert a 3×3 convolutional operation with the padding size of 1 between the first MLP layer and the GELU [33] operation. As a result, we remove the positional encoding in the traditional FFN since the convolutional operation already incorporates positional information. We formulate the convolutional feed-forward network (C-FFN) as:

$$\hat{F}_i = \text{MLP}(C_i, C_{\text{expand}})(\text{IN}(F_i)), \forall i, \quad (3)$$

$$\hat{F}_i = \text{Conv}_{3 \times 3}(C_{\text{expand}}, C_{\text{expand}})(\hat{F}_i), \forall i, \quad (4)$$

$$\hat{F}_i = \text{GELU}(\hat{F}_i), \forall i, \quad (5)$$

$$\hat{F}_i = \text{MLP}(C_{\text{expand}}, C_i)(\hat{F}_i) + F_i, \forall i, \quad (6)$$

where C_{expand} represents the expanded feature dimension of the feed-forward network [21], and $\{\hat{F}_i | i = 1, 2, 3, 4\}$ denotes the output pyramid feature maps of the C-FFN module. We set the expansion ratio of each stage to $[8, 8, 4, 4]$.

2) *MLP Decoder*: We design a simple decoder to generate the unified appearance representations of the object instance from the pyramid features obtained from the multi-scale transformer encoder. First, the pyramid features $\{\hat{F}_i | i = 1, 2, 3, 4\}$ are passed through an MLP layer to unify the channel dimensions to be consistent with the maximum feature channel C_4 . Then, the unified feature maps are up-sampled to $1/4$ size of the original input image and concatenated along the feature channel to form $\frac{H}{4} \times \frac{W}{4} \times 4C_4$. Later on, an MLP layer is used to fuse the concatenated features to $\frac{H}{4} \times \frac{W}{4} \times C_4$. Next, the

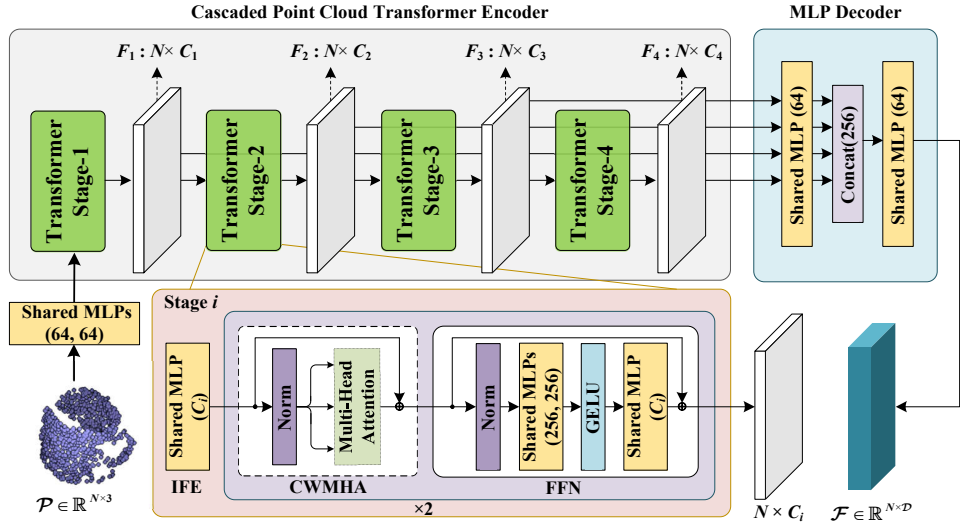


Fig. 3. The structure of the proposed Pointformer. The network consists of two main modules: a cascaded transformer encoder with different feature dimensions to capture multi-level point embeddings; and an all-MLP decoder to unify and fuse the multi-level point embeddings and produce the pointwise object geometric representations. Note that in the figure, each item in the format of $Function(\cdot, \dots, \cdot)$ denotes the feature dimension after the corresponding operation.

fused features are passed through two alternative up-sampling and MLP layers to get the unified appearance representations. We formulate the process of the MLP decoder as follows:

$$\hat{F}_i = \text{MLP}(C_i, C_4)(\hat{F}_i), \forall i, \quad (7)$$

$$\hat{F}_i = \text{UpSample}(H_i \times W_i, \frac{H}{4} \times \frac{W}{4})(\hat{F}_i), \forall i, \quad (8)$$

$$\hat{F} = \text{MLP}(4C_4, C_4)(\text{Concat}(\hat{F}_i)), \forall i, \quad (9)$$

$$\hat{F} = \text{UpSample}(\frac{H}{4} \times \frac{W}{4}, \frac{H}{2} \times \frac{W}{2})(\hat{F}), \quad (10)$$

$$\hat{F} = \text{MLP}(C_4, 2D)(\hat{F}), \quad (11)$$

$$\hat{F} = \text{UpSample}(\frac{H}{2} \times \frac{W}{2}, H \times W)(\hat{F}), \quad (12)$$

$$F = \text{MLP}(2D, D)(\text{MLP}(2D, 2D)(\hat{F})), \quad (13)$$

where F refers to the output pixelwise instance appearance representations with the shape as $H \times W \times D$, where D is the output dimension, which is set as 32 to be consistent with previous appearance extractors [10], [17]. Additionally, for the $\text{UpSample}(b, c)(a)$ operation, we utilize the simple bilinear interpolation to recover the details of the origin feature map. The design details of Pixelformer can be found in TABLE I.

TABLE I
DETAILED SETTINGS OF THE PROPOSED PIXELFORMER FOR INSTANCE REPRESENTATION LEARNING ON RGB IMAGES.

| Param Name | Stage I | | | |
|---------------------------------|---------|---------|---------|---------|
| | 1 | 2 | 3 | 4 |
| Number of Attention Heads M | 1 | 2 | 5 | 8 |
| FFN Expansion Ratio R_{FFN} | 8 | 8 | 4 | 4 |
| Feature Channels C | 32 | 64 | 160 | 256 |
| Expanded Dimension C_{expand} | 256 | 512 | 640 | 1024 |
| Reduction Ratio R | 8 | 4 | 2 | 1 |
| Patch Window Size (K, S, P) | (7,4,3) | (3,2,1) | (3,2,1) | (3,2,1) |
| Number of Transformers L | 2 | 2 | 2 | 2 |

C. Instance Representation Learning on Point Clouds

Due to the disorder and irregularity of 3D point clouds, deep representation learning on point clouds is very challenging. Moreover, the operations on point clouds must be permutation-invariant, which makes this problem more difficult [34]. The recent transformer architecture [21] and its core component — self-attention mechanism, not only meet the demand for permutation-invariance, but also have been proven to be highly expressive in modeling long-range dependencies between different elements within a sequence of data. Therefore, it is an ideal choice to adapt the transformer architectures to point cloud processing. Nevertheless, only a few studies [24], [35], [36] have made this attempt, and existing networks suffer from growing memory requirement, as well as highly computational consumption. To address this problem, we design a simple but effective transformer-based 3D point cloud learning network called Pointformer, suitable for learning the geometric representations of the object instance.

As illustrated in Fig. 3, given an input point cloud \mathcal{P} with N points, before the main network starts, we first perform two layers of shared MLPs to map the raw points to the d -dimensional feature description. Then, similar to Pixelformer, our Pointformer is also an encoder-decoder network which contains two main components: 1) a cascaded transformer encoder includes I ($I = 4$) stages with different dimensions to capture multi-level point embeddings; 2) an all-MLP decoder to unify and fuse the multi-level embeddings to produce the pointwise geometric representations of the object instance.

1) *Cascaded Transformer Encoder*: At each stage i , $i \in \{1, 2, 3, 4\}$, it has an input embedding layer (IFE) that maps the d -dimensional feature description to the corresponding embedded dimension C_i , followed by two layers of alternating channel-wise multi-head attention (CWMHA) and feed-forward network (FFN) to model the long-range context interactions among points, and further improve the point

representations, respectively.

a) *Input Feature Embedding*: There are many input feature embedding methods in the literature [35], which is not covered in this work. For sake of simplicity, we directly apply an MLP layer to the d -dimensional feature description to obtain pointwise embeddings with dimension of C_i , where $i \in \{1, 2, 3, 4\}$. Thus, we can obtain the multi-level point embeddings with the shape of $\{\mathcal{F}_i | i = 1, 2, 3, 4\} = \{N \times C_1, N \times C_2, N \times C_3, N \times C_4\}$.

b) *Channel-wise Multi-head Attention*: In order to highlight the interactions across different embedding channels, we build a channel-wise multi-head attention module to enhance the contextual point representations. Specifically, let $Q_i, K_i, V_i = \text{MLP}(C_i, C_i)(\mathcal{F}_i)$, $i \in \{1, 2, 3, 4\}$ be the *query*, *key* and *value* vectors at each stage i , and each head of Q_i, K_i, V_i has the same shape of $N \times d_{\text{head}(i)}$, where $d_{\text{head}(i)} = C_i/M_i$, M_i denotes the number of attention heads, and N is the number of points. Therefore, the channel-wise multi-head attention operation is formally defined as

$$A_i = \text{Softmax}\left(\frac{Q_i K_i^T}{\sqrt{d_{\text{head}(i)}}}\right), \forall i, \quad (14)$$

$$\text{Attention}(Q_i, K_i, V_i) = A_i V_i, \forall i, \quad (15)$$

here, $A_i \in \mathbb{R}^{C_i \times C_i}$ denotes the attention weights between channels, which captures the channel-wise importance. Since Q_i, K_i, V_i in Eq.(14) are determined by linear transformations and the input multi-level point embeddings $\mathcal{F}_i, i \in \{1, 2, 3, 4\}$, they are all order-independent. In addition, the softmax function in Eq.(14) and the weighed sum operation in Eq. (15) are both permutation-invariant. Therefore, the channel-wise multi-head attention mechanism is permutation-invariant, making it suitable for disordered, and irregular point clouds processing.

c) *Feed-Forward Network*: We utilize the instance normalization operation, the GELU [33] activation function, and MLPs to form the feed-forward network in our Pointformer, the process is defined as,

$$\hat{\mathcal{F}}_i = \text{MLP}(C_i, C_{\text{expand}})(\text{IN}(\mathcal{F}_i)), \forall i, \quad (16)$$

$$\hat{\mathcal{F}}_i = \text{MLP}(C_{\text{expand}}, C_{\text{expand}})(\hat{\mathcal{F}}_i), \forall i, \quad (17)$$

$$\hat{\mathcal{F}}_i = \text{GELU}(\hat{\mathcal{F}}_i), \forall i, \quad (18)$$

$$\hat{\mathcal{F}}_i = \text{MLP}(\mathcal{F}_i) + \mathcal{F}_i, \forall i. \quad (19)$$

Where C_{expand} represents the expanded embedding dimension of the feed-forward network [21], and $\{\hat{\mathcal{F}}_i | i = 1, 2, 3, 4\}$ denotes the output multi-level point embeddings of the FFN module. To be consistent with Pixelformer, we set the expansion ratio of each stage as $[8, 8, 4, 4]$.

2) *All-MLP Decoder*: We design a simple all-MLP decoder to generate the pointwise geometric representations of the object instance from the multi-level point embeddings created by the cascaded transformer encoder. First of all, the multi-level point embeddings $\{\hat{\mathcal{F}}_i | i = 1, 2, 3, 4\}$ are fed into four separate MLP layers to unify the different channel dimensions to \mathcal{D} . Secondly, the unified point embeddings are concatenated to produce new point embeddings with the shape of $N \times 4\mathcal{D}$.

Finally, an MLP layer is applied to project the concatenated point embeddings to \mathcal{D} -dimensional feature description. We formulate the process of the decoder as follows:

$$\hat{\mathcal{F}}_i = \text{MLP}(C_i, \mathcal{D})(\hat{\mathcal{F}}_i), \forall i, \quad (20)$$

$$\hat{\mathcal{F}} = \text{Concat}(\hat{\mathcal{F}}_i), \forall i, \quad (21)$$

$$\mathcal{F} = \text{MLP}(4\mathcal{D}, \mathcal{D})(\hat{\mathcal{F}}), \quad (22)$$

where \mathcal{F} refers to the output pointwise geometric embedding with the shape of $N \times \mathcal{D}$, and \mathcal{D} is the output dimension, which is set as 64 to be consistent with previous geometric extractors [10], [17]. The design details of Pointformer can be found in TABLE II.

TABLE II
DETAILED SETTINGS OF THE PROPOSED POINTFORMER FOR INSTANCE REPRESENTATION LEARNING ON POINT CLOUDS.

| Param Name | Stage I | | | |
|--|---------|-----|-----|------|
| | 1 | 2 | 3 | 4 |
| Number of Attention Heads M | 1 | 2 | 5 | 8 |
| FFN Expansion Ratio R_{FFN} | 8 | 8 | 4 | 4 |
| Feature Channels C | 32 | 64 | 160 | 256 |
| Expanded Dimension C_{expand} | 256 | 512 | 640 | 1024 |
| Number of Transformers L | 2 | 2 | 2 | 2 |

D. Joint and Dense Representation Generation and Pose Estimation

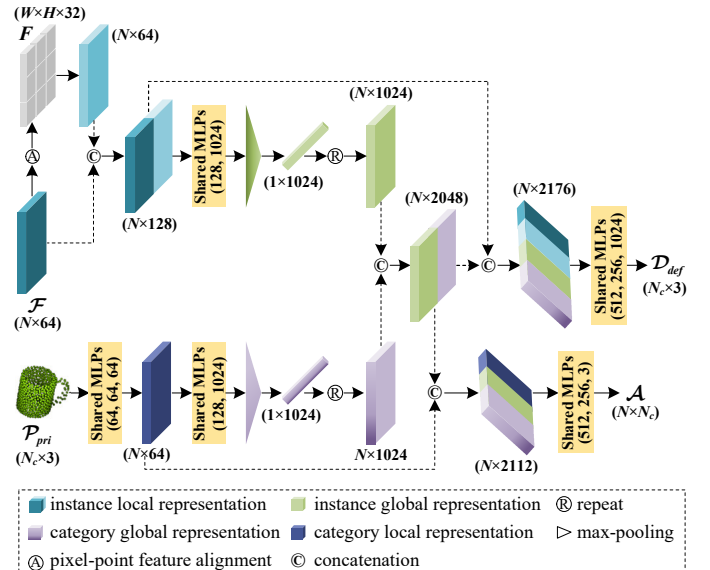


Fig. 4. The structure of the multi-source aggregation network (MSA). The network takes the pixelwise appearance representations, the pointwise geometric representations, and the categorical shape priors as input, and outputs the dense instance representations (e.g., correspondence matrix and deformation field) used to calculate the 6D object pose.

We utilize a multi-source aggregation network (MSA) to unify and generate the dense instance representations as suggested in SPD [17] (i.e., deformation field, correspondence matrix) regarding to the pixelwise appearance representations $F \in \mathbb{R}^{H \times W \times D}$, the pointwise geometric representations

$\mathcal{F} \in \mathbb{R}^{N \times D}$, and the categorical shape priors $\mathcal{P}_{pri} \in \mathbb{R}^{N_c \times 3}$ provided by SPD [17], where N_c is the number of points in the shape priors.

As shown in Fig. 4, the MSA contains two parallel branches. In the upper branch, we associate the appearance representations F with the geometric representations \mathcal{F} according to the natural pixel-to-point correspondence. Besides, in order to unify the feature dimensions of these two modalities, an MLP layer is applied. After that, the aligned cross-modality representations are concatenated and termed *instance local representation*, and fed into a shared MLPs, followed by an average pooling layer to obtain the *instance global representation*. In the lower branch, the categorical shape priors \mathcal{P}_{pri} are utilized to provide the prior knowledge of each category. Specifically, we employ two shared MLPs to extract the *category local representation* and the *category global representation* from the shape priors, respectively. Then, the two category-level representations are concatenated, and enriched either by the *category local representation* followed by a shared MLPs to generate the deformation field $\mathcal{D}_{def} \in \mathbb{R}^{N_c \times 3}$ from the categorical shape priors to a particular instance canonical model, or by the *instance local representation* followed by another shared MLPs to generate the correspondence matrix $\mathcal{A} \in \mathbb{R}^{N \times N_c}$, which represents the soft correspondence between each point in the input instance point cloud \mathcal{P} and all points in the reconstructed instance model $\hat{\mathcal{P}}$, where $\hat{\mathcal{P}} = \mathcal{P}_{pri} + \mathcal{D}_{def}$. Finally, the NOCS coordinates of the instance point cloud, denoted as $\hat{\mathcal{M}}$, are obtained by multiplying the correspondence matrix \mathcal{A} and the reconstructed object model $\hat{\mathcal{P}}$, *i.e.*,

$$\hat{\mathcal{M}} = \mathcal{A} \times \hat{\mathcal{P}}. \quad (23)$$

Given the instance point cloud \mathcal{P} with its corresponding NOCS coordinates $\hat{\mathcal{M}}$, we use the Umeyama algorithm [31] to estimate the optimal similarity transformation parameters (*a.k.a.*, rotation, translation, and scale), where the rotation and translation parameters correspond to the 6D object pose, and the scale parameter corresponds to the object size. The RANSAC algorithm [37] is also adopted to remove outliers and achieve robust estimation.

E. Loss Functions

We utilize the same loss functions as suggested in SPD [17] to supervise different components of our method.

1) *Reconstruction Loss*: We employ the Chamfer distance to measure the similarity between the ground truth 3D model and the reconstructed 3D model, which is defined as

$$L_{cd}(\hat{\mathcal{P}}_c^i, \mathcal{P}_c^i) = \sum_{x \in \mathcal{P}_c^i} \min_{y \in \hat{\mathcal{P}}_c^i} \|x - y\|_2^2 + \sum_{y \in \hat{\mathcal{P}}_c^i} \min_{x \in \mathcal{P}_c^i} \|x - y\|_2^2, \quad (24)$$

where \mathcal{P}_c^i is the ground truth 3D point cloud model of instance i from category c , and $\hat{\mathcal{P}}_c^i$ is its corresponding reconstructed 3D point cloud model. Since the reconstructed model is derived by the categorical shape priors and deformation field, *i.e.*, $\hat{\mathcal{P}} = \mathcal{P}_{pri} + \mathcal{D}_{def}$, therefore, the regression of the deformation field is also implicitly supervised by the reconstruction loss.

2) *Correspondence Loss*: We follow SPD [17] to supervise the deformation field \mathcal{D}_{def} indirectly by supervising the NOCS coordinates $\hat{\mathcal{M}}$ with the smooth L_1 loss function,

$$\hat{L}_{cor}(m, m_{gt}) = \begin{cases} 5(m - m_{gt})^2, & |m - m_{gt}| \leq 0.01 \\ |m - m_{gt}| - 0.05, & \text{otherwise} \end{cases}, \quad (25)$$

$$L_{cor}(\hat{\mathcal{M}}, \mathcal{M}) = \frac{1}{N} \sum_{m \in \hat{\mathcal{M}}} \hat{L}_{cor}(m, m_{gt}), \quad (26)$$

where m_{gt} is the ground truth NOCS coordinate from \mathcal{M} , and m is the predicted NOCS coordinate from $\hat{\mathcal{M}}$. Therefore, the correspondence loss is computed as the average correspondence loss over all the NOCS coordinates.

3) *Regularization Losses*: In order to penalize large deformations and constrain the correspondence matrix \mathcal{A} to be sparse, we impose two regularization losses to each point d_i in the deformation field, and each raw \mathcal{A}_i of the correspondence matrix, respectively.

$$L_{def} = \frac{1}{N_c} \sum_{d_i \in \mathcal{D}_{def}} \|d_i\|_2, \quad (27)$$

$$L_{spar} = \frac{1}{N} \sum_i \sum_j -\mathcal{A}_{i,j} \log \mathcal{A}_{i,j}. \quad (28)$$

To sum up, the overall loss function is a weighted sum of all the four loss functions:

$$L = \lambda_1 L_{cd} + \lambda_2 L_{cor} + \lambda_3 L_{def} + \lambda_4 L_{spar}. \quad (29)$$

IV. EXPERIMENTS

In this section, we conduct extensive experiments on two state-of-the-art benchmark datasets (*i.e.*, CAMERA25 [18] and REAL275 [18]) to evaluate the performance of the presented method, and compare our results with the baseline approach [17] and other state of the arts. We have also provided a comprehensive ablation analysis (18 experiments in total) to verify the perspective advantages of the proposed Pixelformer and Pointformer of our framework, and compare each of them with latest state-of-the-art transformer-based appearance [22] or geometric [24] representation generators. Furthermore, we show the visualization results of the pose estimation results and the 3D object models reconstructed by our network, which qualitatively demonstrate the effectiveness of our approach.

A. Datasets

The CAMERA25 and REAL275 datasets are both collected by NOCS [18] which contains six different categories: bottle, bowl, camera, can, laptop and mug. Specifically, the CAMERA25 dataset is generated by rendering and compositing synthetic object instances from ShapeNet-Core [38] under different views. In this situation, the training set covers 1,085 object instances, while the evaluation set covers 184 different instances. In total, it contains 300K composite RGB-D images, where 25K are set aside for evaluation. The REAL275 [18]

TABLE III
CATEGORY-WISE RESULTS OF OUR NETWORK ON THE CAMERA25 AND REAL275 DATASETS UNDER DIFFERENT EVALUATION METRICS.

| Dataset | Category | 3D ₅₀ | 3D ₇₅ | 5°2cm | 5°5cm | 10°2cm | 10°5cm | 10° 10cm |
|----------|----------|------------------|------------------|--------|--------|--------|--------|----------|
| CAMERA25 | Bottle | 0.9242 | 0.8524 | 0.7357 | 0.8962 | 0.7591 | 0.9436 | 0.9760 |
| | Bowl | 0.9668 | 0.9563 | 0.9396 | 0.9430 | 0.9727 | 0.9801 | 0.9810 |
| | Camera | 0.9114 | 0.8228 | 0.4942 | 0.5018 | 0.7109 | 0.7374 | 0.7383 |
| | Can | 0.9181 | 0.9108 | 0.9508 | 0.9552 | 0.9632 | 0.9741 | 0.9760 |
| | Laptop | 0.9576 | 0.8619 | 0.7131 | 0.7801 | 0.7790 | 0.8897 | 0.9316 |
| | Mug | 0.9297 | 0.9048 | 0.5252 | 0.5258 | 0.7527 | 0.7538 | 0.7539 |
| | Average | 0.9346 | 0.8849 | 0.7265 | 0.7670 | 0.8229 | 0.8798 | 0.8928 |
| Dataset | Category | 3D ₅₀ | 3D ₇₅ | 5°2cm | 5°5cm | 10°2cm | 10°5cm | 10° 10cm |
| REAL275 | Bottle | 0.5766 | 0.5005 | 0.5799 | 0.6318 | 0.7969 | 0.8703 | 0.9452 |
| | Bowl | 0.9999 | 0.9992 | 0.7874 | 0.8186 | 0.9548 | 0.9914 | 0.9914 |
| | Camera | 0.8709 | 0.1917 | 0.0000 | 0.0000 | 0.0014 | 0.0019 | 0.0019 |
| | Can | 0.7146 | 0.6996 | 0.5350 | 0.5624 | 0.8573 | 0.9551 | 0.9555 |
| | Laptop | 0.8334 | 0.6170 | 0.3383 | 0.4461 | 0.6163 | 0.9217 | 0.9361 |
| | Mug | 0.9878 | 0.8577 | 0.0490 | 0.0524 | 0.3166 | 0.3333 | 0.3333 |
| | Average | 0.8306 | 0.6443 | 0.3816 | 0.4186 | 0.5906 | 0.6789 | 0.6989 |

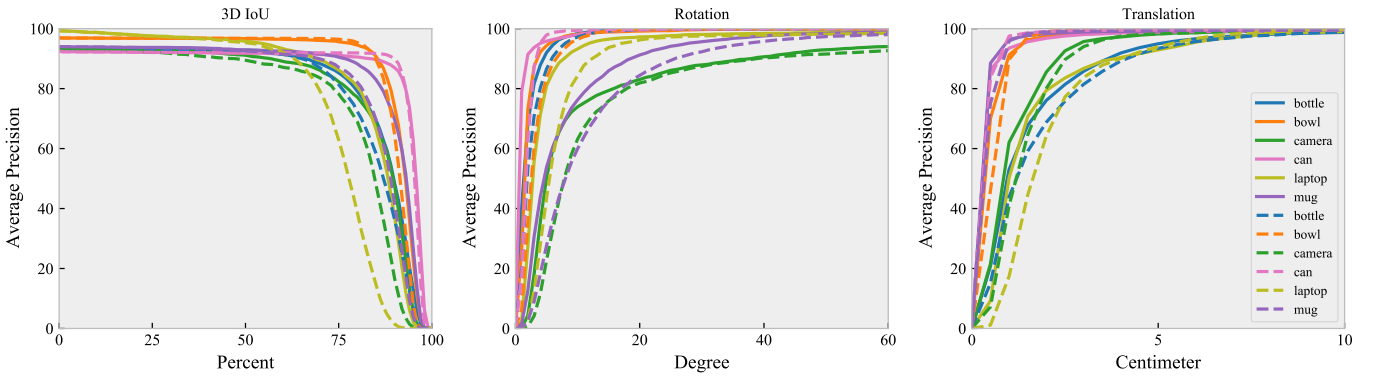


Fig. 5. Category-level comparison with the baseline method: SPD [17] on the CAMERA25 dataset. Solid line denotes the results of our 6D-ViT, dashed line denotes the results of SPD [17]. We report the precision of different thresholds with 3D IoU, rotation and translation error.

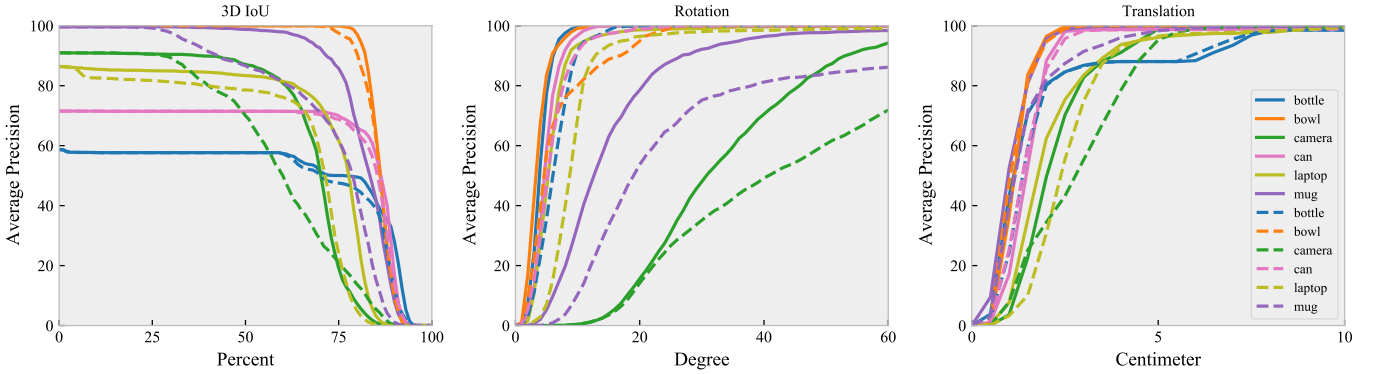


Fig. 6. Category-level comparison with SPD [17] on the REAL275 dataset. Solid line denotes the results of our 6D-ViT, dashed line denotes the results of SPD [17]. We report the precision of different thresholds with 3D IoU, rotation and translation error.

dataset is complementary to the CAMERA25 dataset. It captures 4,300 real-world images of 7 scenes for training, and 2,750 real-world images of 6 scenes with 3 unseen instances per category for evaluation. Both the training set and testing set contains 18 real object instance spanning the 6 categories.

B. Metrics

Following [13]–[18], we independently evaluate the performance of our method in 3D object detection and 6D object pose estimation, and compare the results with state of the

arts. For 3D object detection, we report the average precision at different Intersection-Over-Union (IoU) thresholds. For 6D object pose estimation, the average precision is computed as $n^\circ m \text{ cm}$. We ignore the rotational error around the axis of symmetry for symmetrical object categories (*e.g.* bottle, bowl, and can). In particular, we regard mugs as symmetric objects in the absence of the handle, and asymmetric objects, otherwise. In addition, the Chamfer distance (Eq. (24)) is employed to evaluate the accuracy of shape reconstruction from single-view RGB-D images.

TABLE IV

QUANTITATIVE COMPARISONS ON THE CAMERA25 AND REAL275 DATASETS. WE REPORT THE MAP w.r.t. DIFFERENT THRESHOLDS ON 3D IoU, AND ROTATION AND TRANSLATION ERRORS. THE RESULTS OF THE COMPARISON METHODS ARE SUMMARIZED FROM THEIR ORIGINAL PAPERS.

| Method | CAMERA25 | | | | | | | REAL275 | | | | | | |
|---------------------------|--------------|--------------|----------------------|----------------------|-----------------------|-----------------------|------------------------|--------------|--------------|----------------------|----------------------|-----------------------|-----------------------|------------------------|
| | IoU_{50} | IoU_{75} | $5^\circ 2\text{cm}$ | $5^\circ 5\text{cm}$ | $10^\circ 2\text{cm}$ | $10^\circ 5\text{cm}$ | $10^\circ 10\text{cm}$ | IoU_{50} | IoU_{75} | $5^\circ 2\text{cm}$ | $5^\circ 5\text{cm}$ | $10^\circ 2\text{cm}$ | $10^\circ 5\text{cm}$ | $10^\circ 10\text{cm}$ |
| NOCS[CVPR'19] [18] | 83.9% | 69.5% | 32.3% | 40.9% | 48.2% | 64.6% | - | 78.0% | 30.1% | 7.2% | 10.0% | 13.8% | 25.2% | 26.7% |
| CASS[CVPR'20] [14] | - | - | - | - | - | - | - | 77.7% | - | - | 23.8% | - | 58.0% | 58.3% |
| NOF[ECCV'20] [13] | - | - | - | - | - | - | - | 76.9% | 30.1% | 7.2% | 9.8% | 13.8% | 24.0% | 24.3% |
| SPD[ECCV'20] [17] | 93.2% | 83.1% | 54.3% | 59.0% | 73.3% | 81.5% | - | 77.3% | 53.2% | 19.3% | 21.4% | 43.2% | 54.1% | - |
| FS-Net[CVPR'21] [15] | - | - | - | - | - | - | - | 92.2% | 63.5% | - | 28.2% | - | 60.8% | 64.6% |
| DualPoseNet[ICCV'21] [16] | 92.4% | 86.4% | 64.7% | 70.7% | 77.2% | 84.7% | - | 79.8% | 62.2% | 29.3% | 35.9% | 50.0% | 66.8% | - |
| 6D-ViT(Ours) | 93.5% | 88.5% | 72.6% | 76.7% | 82.3% | 88.0% | 89.3% | 83.1% | 64.4% | 38.2% | 41.9% | 59.1% | 67.9% | 69.9% |

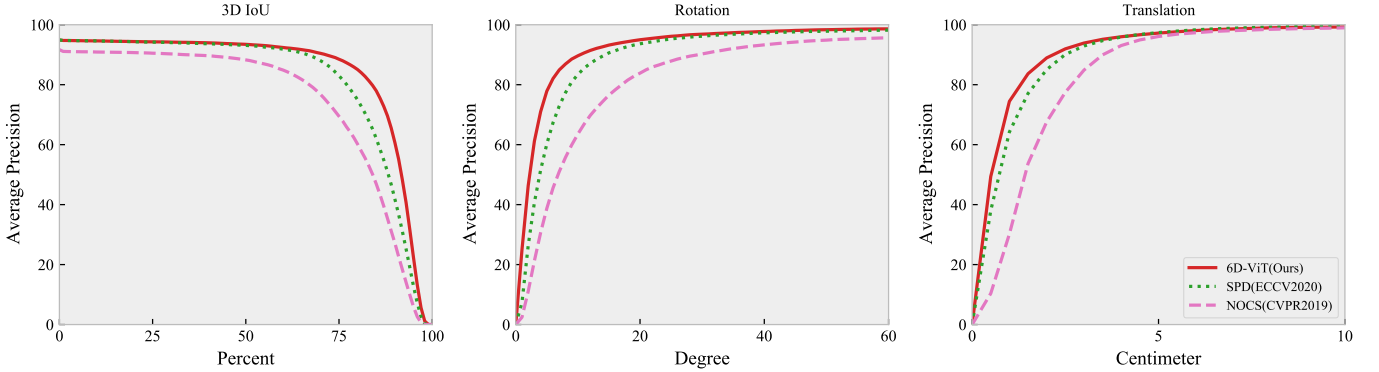


Fig. 7. The average precision of all categories on the CAMERA25 dataset. We present different thresholds with 3D IoU, rotation and translation errors.

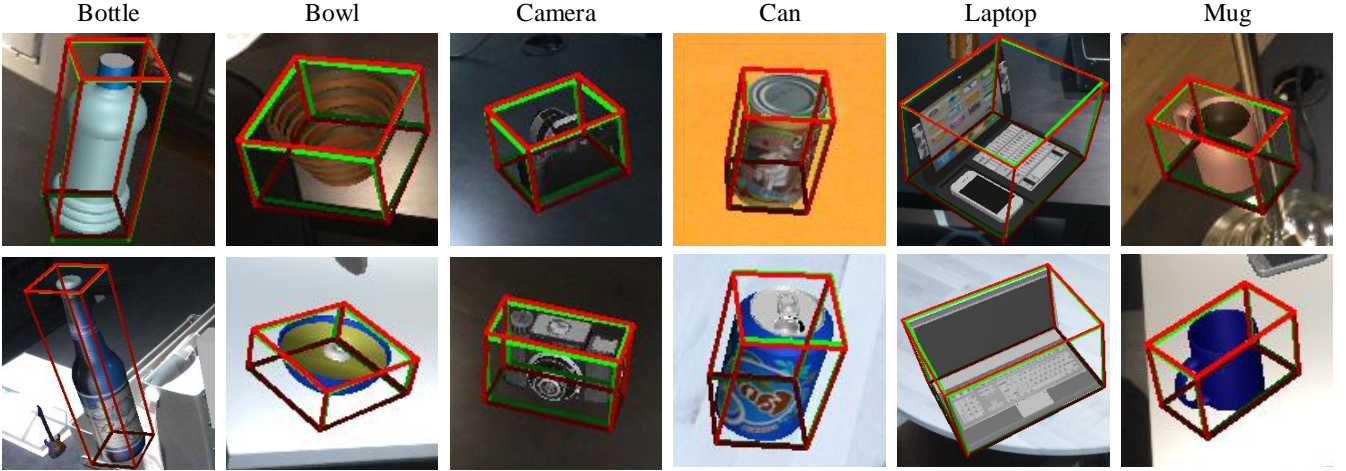


Fig. 8. The visualization of 6D object poses on the CAMERA25 dataset. Green bounding boxes denote the ground truth. Red boxes denote our estimations. Our results match the ground truth well in both pose and size.

C. Implementation Details

We use Pytorch [39] framework to implement our method, and the state-of-the-art framework SPD [17] is developed as the baseline. All the experiments are conducted on a PC with i9-10900K 3.70GHz CPU and two GTX 2080Ti GPUs. The RGB image is cropped and resized to 256×256 . The number of points in the instance point clouds and categorical shape priors is set as 1,024. We adopt Adam [40] to optimize our network, where the initial learning rate is set as $1e-4$, and we halve it every 20 epochs with a weight decay of $1e-6$. The maximum epoch is 100. For the hyper-parameters of the loss function (Eq. (29)), we follow SPD [17] to set $\lambda_1 = 5.0$, $\lambda_2 = 1.0$, $\lambda_3 = 1.0$, and $\lambda_4 = 1e-4$.

D. Evaluation of 6D Object Pose Estimation

We evaluate the performance of our 6D object pose estimation network: 6D-ViT, on two widely used benchmark datasets (*i.e.*, CAMERA25 and REAL275), and compare our results with the baseline method: SPD [17], and five other state-of-the-art methods, including NOCS [18], CASS [14], NOF [13], FS-Net [15], and DualPoseNet [16]. As far as we know, these are all the popular methods in the current literature to solve the challenging category-level 6D object pose estimation problem.

1) *Comparison with Baseline*: In order to verify the effectiveness of our method, we report the category-specific precision of our 6D-ViT on the CAMERA25 and REAL275 datasets under different thresholds with 3D IoU, rotation and

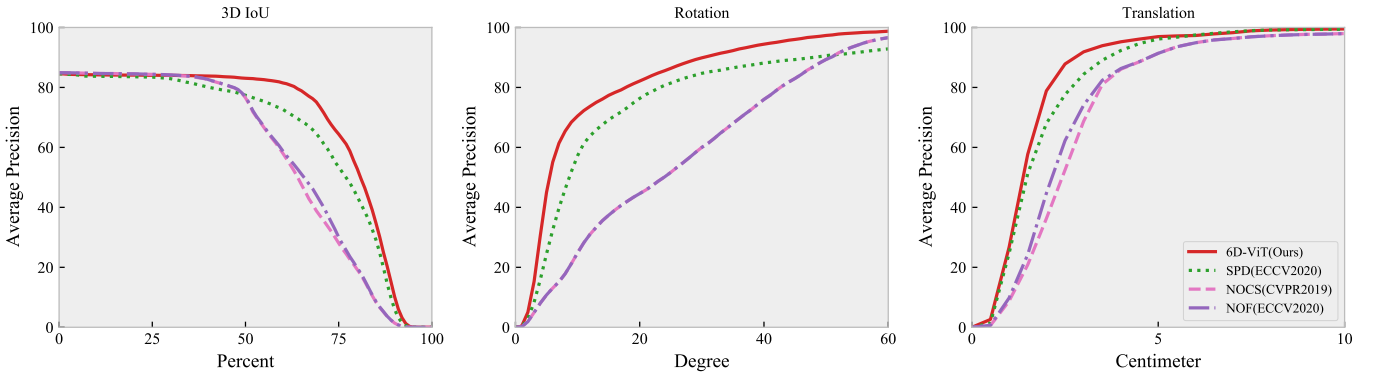


Fig. 9. The average precision of all categories on the REAL275 dataset. We present different thresholds with 3D IoU, rotation and translation errors.

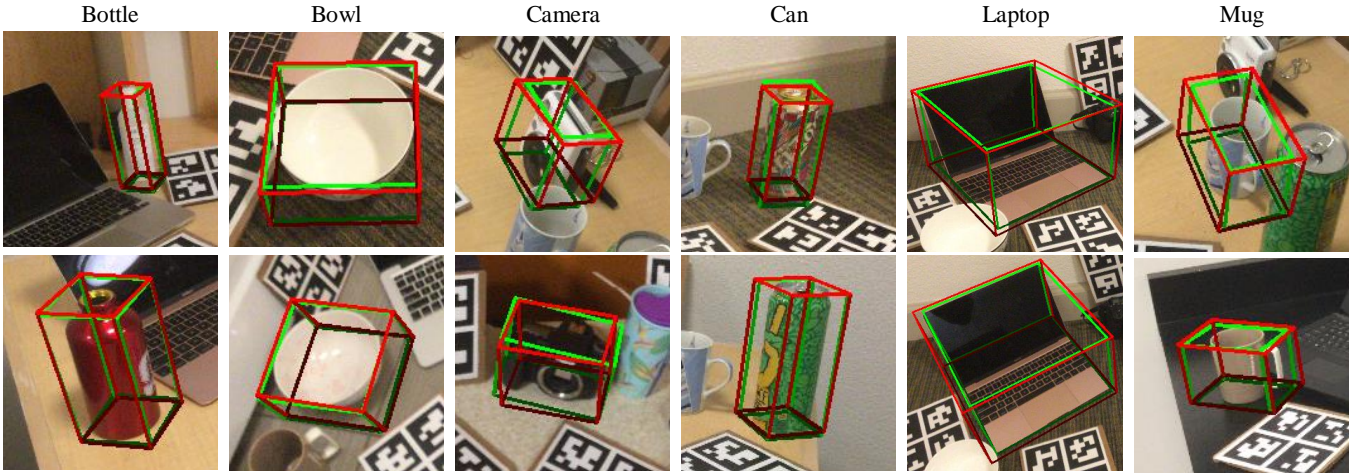


Fig. 10. The visualization of 6D object poses on the REAL275 dataset. Green bounding boxes denote the ground truth. Red boxes denote our estimations. Our results match the ground truth well in both pose and size.

translation errors, and compare all results with SPD [17]. The comparisons can be found in Fig. 5 and Fig. 6, respectively. It can be seen from the results that for all evaluation metrics, our method has achieved a remarkable performance improvement compared with the baseline method in each category of the two datasets. In addition, we also provide detailed category-specific results under several widely used thresholds to show our results more intuitively. The results are provided in TABLE III.

2) *Comparison with State of the Arts*: To further validate the competitiveness of our method, we compare the average precision of 6D-ViT with that of NOCS [18], CASS [14], NOF [13], SPD [17], FS-Net [15], and DualPoseNet [16] on both the CAMERA25 and REAL275 datasets. The results are reported in TABLE IV.

a) *CAMERA25*: As shown in TABLE IV-left, our 6D-ViT is superior to all existing methods on the CAMERA25 dataset. Specifically, for 3D object detection metrics: IoU_{50} and IoU_{75} , our 6D-ViT outperforms the previous best method, DualPoseNet [16], by 1.1% and 2.1%, respectively. In terms of 6D pose metrics: $5^{\circ}2\text{cm}$, $5^{\circ}5\text{cm}$, $10^{\circ}2\text{cm}$ and $10^{\circ}5\text{cm}$, 6D-ViT has advantages of 7.9%, 6.0%, 5.1%, and 3.3% respectively, which is significantly better than DualPoseNet [16]. Furthermore, 6D-ViT achieves an average precision of 89.3% under the $10^{\circ}10\text{cm}$ metric. We show more detailed quantitative

comparisons in Fig. 7, and our qualitative results on the CAMERA25 dataset are shown in Fig. 8.

b) *REAL275*: As shown in TABLE IV-right, it can be observed that our proposed 6D-ViT is superior to the existing methods under all evaluation metrics except for IoU_{50} , which is a rather rough metric. Specifically, for 3D object detection, FS-Net [15] is the current best method under the IoU_{50} metric, and our 6D-ViT has achieved the second best average precision of 83.1%, which is 9.1% lower than that of FS-Net [15]. However, under the more difficult IoU_{75} metric, the performance of our 6D-ViT is 0.9% higher than that of FS-Net [15]. As for the 6D pose evaluation metrics: $5^{\circ}2\text{cm}$, $5^{\circ}5\text{cm}$, $10^{\circ}2\text{cm}$ and $10^{\circ}5\text{cm}$, our 6D-ViT significantly outperforms the previous best method, DualPoseNet [16] by 8.9%, 6.0%, 9.1%, 1.1%, respectively. In addition, 6D-ViT achieves an average accuracy of 69.9% under the $10^{\circ}10\text{cm}$ metric, which is 5.3% higher than the best result previously reported.

We believe that the performance gap between our method and FS-Net [15] in 3D object detection is because FS-Net [15] utilizes YOLOv3 [41] to crop object instances from RGB-D images, while our method along with other methods employ Mask-RCNN [30] instead. More specifically, YOLOv3 has a higher success rate for coarse instance detection, while Mask R-CNN is better at more accurate instance localization.

TABLE V
EVALUATION OF THE 3D MODEL RECONSTRUCTION USING THE CD METRIC ($\times 10^{-3}$).

| Method | CAMERA | | | | | | REAL275 | | | | | | | |
|---------------|-------------|-------------|-------------|-------------|-------------|-------------|-------------|-------------|-------------|-------------|-------------|-------------|-------------|-------------|
| | Bottle | Bowl | Camera | Can | Laptop | Mug | Average | Bottle | Bowl | Camera | Can | Laptop | Mug | |
| Baseline [17] | 1.81 | 1.63 | 4.02 | 0.97 | 1.98 | 1.42 | 1.97 | 3.44 | 1.21 | 8.89 | 1.56 | 2.91 | 1.02 | |
| Ours | 1.38 | 1.18 | 2.86 | 0.90 | 1.24 | 1.17 | 1.46 | 2.37 | 1.14 | 6.06 | 1.60 | 1.39 | 1.06 | 2.27 |

TABLE VI

THE ALTERNATIVES OF INSTANCE APPEARANCE FEATURE EXTRACTORS AND INSTANCE GEOMETRIC FEATURE EXTRACTORS USED TO VERIFY THE EFFICACY OF INDIVIDUAL COMPONENTS OF OUR NETWORK.

| | | | |
|------------|-----------|----------|-----------|
| Appearance | PSP [17] | PVT [22] | PIF(Ours) |
| Geometry | MLPs [17] | PT [24] | POF(Ours) |

Therefore, FS-Net [15] performs better than our 6D-ViT under the IoU_{50} metric due to the effectiveness of object detection, while our 6D-ViT outperforms FS-Net [15] under the harder IoU_{75} metric, which validates the advantage of our instance representation learning framework. We show more detailed quantitative comparisons on the REAL275 dataset in Fig. 9, and our qualitative results are provided in Fig. 10.

In summary, our proposed instance representation learning network has achieved the best performance in both 6D object pose estimation and 3D object detection compared to existing category-level pose estimation networks. The excellent performance further reflects the high competitiveness of our 6D-ViT.

E. Evaluation of Model Reconstruction

We calculate the Chamfer distance (as defined in Eq. (24)) between our reconstructed object models $\hat{\mathcal{P}}$ and the ground truth object models \mathcal{P} in the canonical space to evaluate the quality of the model reconstruction. The results and comparisons with SPD [17] are reported in TABLE V. It is observed that the 3D models reconstructed by our 6D-ViT obtain an average CD metric of 1.46 on the CAMERA25 dataset and 2.27 on the REAL275 dataset, compared to 1.97 and 3.17 respectively of the baseline. Better CD metrics indicate that the proposed instance representation learning framework improves the quality of the 3D model reconstruction. We also show a qualitative comparison between the 3D models reconstructed by our network and SPD [17] for the CAMERA25 dataset in Fig. 11 and for the REAL275 dataset in Fig. 12.

From both the quantitative and qualitative perspectives, our 6D-ViT can steadily improve the reconstruction accuracy of the the baseline [17] over all categories on the CAMERA25 dataset and four out of six categories on the REAL275 dataset (the remaining two categories also achieve comparable performance). These analyses reveal that the instance representation learning framework we proposed can not only improve the performance of 6D object pose estimation, but also facilitate the reconstruction of canonical 3D object models.

F. Ablation Analysis

We conduct 18 ablation studies on the CAMERA25 and REAL275 datasets to investigate the efficiency of individual components proposed in 6D-ViT. Specifically, we compare

the proposed Pixelformer and Pointformer of our network with latest state-of-the-art transformer-based appearance [22] or geometric [24] feature generators as well as the feature extractors utilized in the baseline method [17]. TABLE VI shows different alternatives of the appearance and geometric feature generators. From the table, “PSP”, “MLP”, “PVT”, “PT”, “PIF”, and “POF” respectively refers to “PSPNet in the baseline [17]”, “linear projection layers in the baseline [17]”, “pyramid vision transformer [22]”, “point transformer [24]”, “Pixelformer in this work”, and “Pointformer in this work”. There are nine combinations in total, the corresponding comparisons are discussed below.

1) *Evaluation of Pixelformer*: To verify the effectiveness of our proposed Pixelformer (PIF), we compare it with two alternative RGB encoders: (1) PSPNet (PSP) with ResNet-18 [32] as the backbone, which is consistent with the baseline method [17]; (2) PVT in [22], like our PIF, it is also a multi-scale transformer structure designed for dense prediction tasks such as object detection and semantic segmentation. It is worth noting that there are a series of PVT models with different scales, we employ PVT-tiny in the experiments since it shares the parameter settings listed in TABLE I as ours.

As shown in TABLE VII, we set the geometric feature generators as MLPs in the baseline [17] or PT in [24] or our proposed POF, and randomly select a backbone from the above encoders as the appearance feature extractor. The results are reported in TABLE VII. As shown in the table, compare ① ② and ⑧, or ⑤ ③ and ⑥, or ④ ⑦ and ⑨, it is observed that regardless of whether the point cloud branch utilizes MLPs or PT or our proposed POF, using our proposed PIF in the RGB branch achieves the best performance. The conclusion can be drawn on both datasets, which demonstrates the effectiveness of our Pixelformer. In addition, among all comparison experiments, our complete model (⑨) is the best.

2) *Evaluation of Pointformer*: Similarly, in order to verify the effectiveness of our proposed Pointformer (POF), we compare it with two alternative point cloud encoders: (1) MLPs with linear projection layers, which is in consistent with the baseline [17]; (2) PT in [24], which is a multi-scale transformer structure designed for point cloud processing. There are many variants of PT, and we adopt the semantic segmentation structure, which demonstrates impressive performance gains in point cloud processing.

As shown in TABLE VII, we set the appearance feature generators as PSP [17] or PVT [22] or our proposed PIF, and randomly select a backbone from the above encoders as the geometric feature extractors. The results are reported in TABLE VII. As shown in the table, compare ① ⑤ and ⑦, or ② ③ and ④, or ⑧ ⑥ and ⑨, it is observed that regardless of whether the RGB branch utilizes PSP or PVT or our proposed

TABLE VII

ABLATION STUDIES ON THE CAMERA25 AND REAL275 DATASETS. “PSP”, “MLP”, “PVT”, “PT”, “PIF”, AND “POF” RESPECTIVELY REFERS TO “PSPNET IN THE BASELINE [17]”, “LINEAR PROJECTION LAYERS IN THE BASELINE [17]”, “PYRAMID VISION TRANSFORMER [22]”, “POINT TRANSFORMER [24]”, “PIXELFORMER IN THIS WORK”, AND “POINTFORMER IN THIS WORK”.

| Method | CAMERA25 | | | | | | | | | | REAL275 | | | | |
|-------------------------|--------------|--------------|-----------------------|-----------------------|------------------------|------------------------|-------------------------|--------------|--------------|-----------------------|-----------------------|------------------------|------------------------|-------------------------|--|
| | IoU_{50} | IoU_{75} | $5^{\circ}2\text{cm}$ | $5^{\circ}5\text{cm}$ | $10^{\circ}2\text{cm}$ | $10^{\circ}5\text{cm}$ | $10^{\circ}10\text{cm}$ | IoU_{50} | IoU_{75} | $5^{\circ}2\text{cm}$ | $5^{\circ}5\text{cm}$ | $10^{\circ}2\text{cm}$ | $10^{\circ}5\text{cm}$ | $10^{\circ}10\text{cm}$ | |
| ① PSP [17] / MLPs [17] | 93.2% | 83.1% | 54.3% | 59.0% | 73.3% | 81.5% | - | 77.3% | 53.2% | 19.3% | 21.4% | 43.2% | 54.1% | - | |
| ② PVT [22] / MLPs [17] | 91.2% | 77.9% | 43.3% | 47.0% | 62.7% | 71.2% | 72.3% | 69.6% | 41.8% | 15.4% | 16.5% | 39.5% | 44.1% | 46.0% | |
| ③ PVT [22] / PT [24] | 91.4% | 84.2% | 60.0% | 64.2% | 75.5% | 82.2% | 83.2% | 80.2% | 56.8% | 27.8% | 31.4% | 48.8% | 60.5% | 62.3% | |
| ④ PVT [22] / POF(Ours) | 91.1% | 83.9% | 63.6% | 67.6% | 77.0% | 82.7% | 84.1% | 76.2% | 53.4% | 32.1% | 35.5% | 51.7% | 61.3% | 63.3% | |
| ⑤ PSP [17] / PT [24] | 93.3% | 87.6% | 60.9% | 65.6% | 77.9% | 85.4% | 86.6% | 79.5% | 58.9% | 29.0% | 32.1% | 52.8% | 61.1% | 62.9% | |
| ⑥ PIF(Ours) / PT [24] | 92.6% | 85.5% | 65.3% | 69.4% | 78.2% | 84.9% | 86.4% | 81.4% | 67.0% | 35.7% | 38.9% | 58.9% | 67.7% | 69.6% | |
| ⑦ PSP [17] / POF(Ours) | 93.4% | 88.0% | 69.5% | 73.8% | 81.1% | 87.1% | 88.6% | 78.4% | 61.4% | 36.1% | 39.1% | 55.9% | 65.1% | 67.1% | |
| ⑧ PIF(Ours) / MLPs [17] | 93.6% | 87.9% | 63.6% | 67.8% | 79.7% | 86.5% | 87.5% | 82.4% | 61.6% | 27.8% | 30.1% | 52.4% | 63.6% | 65.6% | |
| ⑨ PIF(Ours) / POF(Ours) | 93.5% | 88.5% | 72.6% | 76.7% | 82.3% | 88.0% | 89.3% | 83.1% | 64.4% | 38.2% | 41.9% | 59.1% | 67.9% | 69.9% | |

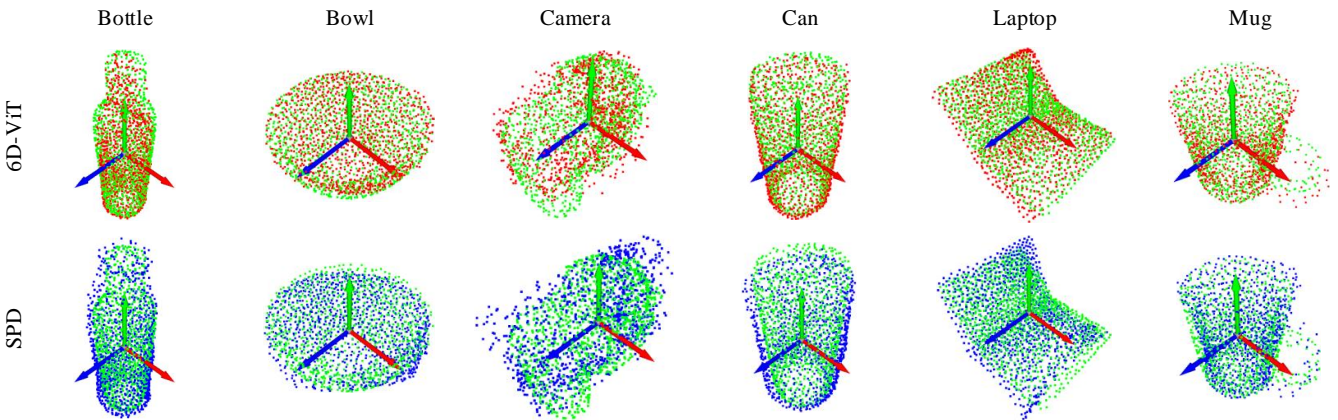


Fig. 11. The visualization of 3D object models reconstructed by our 6D-ViT and SPD [17] on the CAMERA25 dataset. The red points represent the results of ours, the blue points represent the results of SPD, and the green points are the ground truth. We align all the results into the same pose.

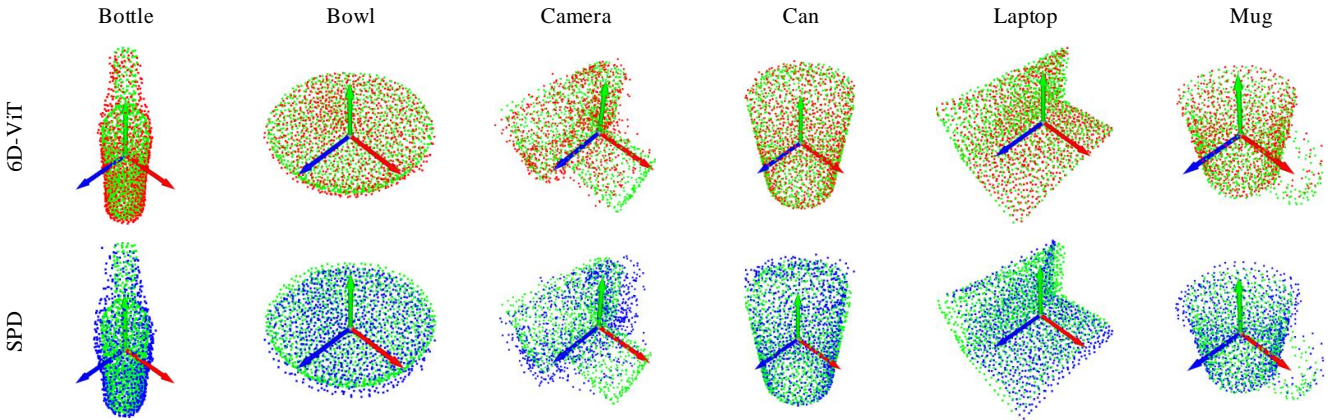


Fig. 12. The visualization of 3D object models reconstructed by our 6D-ViT and SPD [17] on the REAL275 dataset. The red points represent the results of ours, the blue points represent the results of SPD, and the green points are the ground truth. We align all the visualization results into the same pose.

PIF, using our proposed POF in the point cloud branch is achieves the best performance. The conclusion can be drawn on both datasets, which demonstrates the effectiveness of our Pixelformer. In addition, among all comparison experiments, our complete model (⑨) is the best.

V. CONCLUSION

This paper has presented a novel instance representation learning framework for category-level 6D object pose estimation. To achieve this goal, two parallel transformer-based

encoder-decoder networks are designed to learn the long-range dependent instance appearance and geometric characteristics from RGB images and point clouds, respectively. Then, the obtained instance features are fused with categorical shape features to generate joint and dense instance representations. Finally, the 6D object pose is obtained from post-alignment by solving the Umeyama algorithm. We have conducted quantitative and qualitative evaluations on two public benchmark datasets to compare the presented method with the state-of-the-art methods. The results demonstrate that the proposed

method has achieved state-of-the-art performance on both datasets, and significantly exceeds existing methods. We have also implemented sufficient ablation experiments to prove the effectiveness of each component of the proposed network. In the future, we will focus on how to more efficiently explore the potential correlations between instance features from different sources, and apply our instance representation learning framework to the instance-level pose estimation problem.

REFERENCES

- [1] S. Hinterstoisser, V. Lepetit, S. Ilic, S. Holzer, G. Bradski, K. Konolige, and N. Navab, “Model based training, detection and pose estimation of texture-less 3d objects in heavily cluttered scenes,” in *Asian conference on computer vision*. Springer, 2012, pp. 548–562.
- [2] W. Kehl, F. Milletari, F. Tombari, S. Ilic, and N. Navab, “Deep learning of local rgb-d patches for 3d object detection and 6d pose estimation,” in *European conference on computer vision*. Springer, 2016, pp. 205–220.
- [3] W. Kehl, F. Manhardt, F. Tombari, S. Ilic, and N. Navab, “Ssd-6d: Making rgb-based 3d detection and 6d pose estimation great again,” in *Proceedings of the IEEE International Conference on Computer Vision*, 2017, pp. 1521–1529.
- [4] A. Krull, E. Brachmann, F. Michel, M. Ying Yang, S. Gumhold, and C. Rother, “Learning analysis-by-synthesis for 6d pose estimation in rgb-d images,” in *Proceedings of the IEEE international conference on computer vision*, 2015, pp. 954–962.
- [5] C. Li, J. Bai, and G. D. Hager, “A unified framework for multi-view multi-class object pose estimation,” in *Proceedings of the European Conference on Computer Vision (ECCV)*, 2018, pp. 254–269.
- [6] F. Michel, A. Kirillov, E. Brachmann, A. Krull, S. Gumhold, B. Savchynskyy, and C. Rother, “Global hypothesis generation for 6d object pose estimation,” in *Proceedings of the IEEE Conference on Computer Vision and Pattern Recognition*, 2017, pp. 462–471.
- [7] S. Peng, Y. Liu, Q. Huang, X. Zhou, and H. Bao, “Pvnet: Pixel-wise voting network for 6dof pose estimation,” in *Proceedings of the IEEE Conference on Computer Vision and Pattern Recognition*, 2019, pp. 4561–4570.
- [8] M. Sundermeyer, Z.-C. Marton, M. Durner, M. Brucker, and R. Triebel, “Implicit 3d orientation learning for 6d object detection from rgb images,” in *Proceedings of the European Conference on Computer Vision (ECCV)*, 2018, pp. 699–715.
- [9] B. Tekin, S. N. Sinha, and P. Fua, “Real-time seamless single shot 6d object pose prediction,” in *Proceedings of the IEEE Conference on Computer Vision and Pattern Recognition*, 2018, pp. 292–301.
- [10] C. Wang, D. Xu, Y. Zhu, R. Martín-Martín, C. Lu, L. Fei-Fei, and S. Savarese, “Densefusion: 6d object pose estimation by iterative dense fusion,” in *Proceedings of the IEEE Conference on Computer Vision and Pattern Recognition*, 2019, pp. 3343–3352.
- [11] Y. Xiang, T. Schmidt, V. Narayanan, and D. Fox, “Posecnn: A convolutional neural network for 6d object pose estimation in cluttered scenes,” *arXiv preprint arXiv:1711.00199*, 2017.
- [12] S. Zakharov, I. Shugurov, and S. Ilic, “Dpod: Dense 6d pose object detector in rgb images,” *arXiv preprint arXiv:1902.11020*, vol. 1, p. 2, 2019.
- [13] X. Chen, Z. Dong, J. Song, A. Geiger, and O. Hilliges, “Category level object pose estimation via neural analysis-by-synthesis,” in *European Conference on Computer Vision*. Springer, 2020, pp. 139–156.
- [14] D. Chen, J. Li, Z. Wang, and K. Xu, “Learning canonical shape space for category-level 6d object pose and size estimation,” in *Proceedings of the IEEE/CVF conference on computer vision and pattern recognition*, 2020, pp. 11973–11982.
- [15] W. Chen, X. Jia, H. J. Chang, J. Duan, L. Shen, and A. Leonardis, “Fs-net: Fast shape-based network for category-level 6d object pose estimation with decoupled rotation mechanism,” in *Proceedings of the IEEE/CVF Conference on Computer Vision and Pattern Recognition*, 2021, pp. 1581–1590.
- [16] J. Lin, Z. Wei, Z. Li, S. Xu, K. Jia, and Y. Li, “Dualposenet: Category-level 6d object pose and size estimation using dual pose network with refined learning of pose consistency,” *arXiv preprint arXiv:2103.06526*, 2021.
- [17] M. Tian, M. H. Ang, and G. H. Lee, “Shape prior deformation for categorical 6d object pose and size estimation,” in *European Conference on Computer Vision*. Springer, 2020, pp. 530–546.
- [18] H. Wang, S. Sridhar, J. Huang, J. Valentin, S. Song, and L. J. Guibas, “Normalized object coordinate space for category-level 6d object pose and size estimation,” in *Proceedings of the IEEE/CVF Conference on Computer Vision and Pattern Recognition*, 2019, pp. 2642–2651.
- [19] C. Sahin, G. Garcia-Hernando, J. Sock, and T.-K. Kim, “Instance-and category-level 6d object pose estimation,” in *RGB-D Image Analysis and Processing*. Springer, 2019, pp. 243–265.
- [20] Y. Liu, G. Sun, Y. Qiu, L. Zhang, A. Chhatkuli, and L. Van Gool, “Transformer in convolutional neural networks,” *arXiv preprint arXiv:2106.03180*, 2021.
- [21] A. Vaswani, N. Shazeer, N. Parmar, J. Uszkoreit, L. Jones, A. N. Gomez, Ł. Kaiser, and I. Polosukhin, “Attention is all you need,” in *Advances in neural information processing systems*, 2017, pp. 5998–6008.
- [22] W. Wang, E. Xie, X. Li, D.-P. Fan, K. Song, D. Liang, T. Lu, P. Luo, and L. Shao, “Pyramid vision transformer: A versatile backbone for dense prediction without convolutions,” *arXiv preprint arXiv:2102.12122*, 2021.
- [23] E. Xie, W. Wang, Z. Yu, A. Anandkumar, J. M. Alvarez, and P. Luo, “Segformer: Simple and efficient design for semantic segmentation with transformers,” *arXiv preprint arXiv:2105.15203*, 2021.
- [24] H. Zhao, L. Jiang, J. Jia, P. Torr, and V. Koltun, “Point transformer,” in *ICCV*, 2021.
- [25] M. Zhu, K. G. Derpanis, Y. Yang, S. Brahmbhatt, M. Zhang, C. Phillips, M. Lecce, and K. Daniilidis, “Single image 3d object detection and pose estimation for grasping,” in *2014 IEEE International Conference on Robotics and Automation (ICRA)*. IEEE, 2014, pp. 3936–3943.
- [26] W. Liu, D. Anguelov, D. Erhan, C. Szegedy, S. Reed, C.-Y. Fu, and A. C. Berg, “Ssd: Single shot multibox detector,” in *European conference on computer vision*. Springer, 2016, pp. 21–37.
- [27] C. Song, J. Song, and Q. Huang, “Hybridpose: 6d object pose estimation under hybrid representations,” in *Proceedings of the IEEE/CVF Conference on Computer Vision and Pattern Recognition*, 2020, pp. 431–440.
- [28] P. J. Besl and N. D. McKay, “Method for registration of 3-d shapes,” in *Sensor fusion IV: control paradigms and data structures*, vol. 1611. International Society for Optics and Photonics, 1992, pp. 586–606.
- [29] L. Zou, Z. Huang, F. Wang, Z. Yang, and G. Wang, “Cma: Cross-modal attention for 6d object pose estimation,” *Computers & Graphics*, vol. 97, pp. 139–147, 2021.
- [30] K. He, G. Gkioxari, P. Dollár, and R. Girshick, “Mask r-cnn,” in *Proceedings of the IEEE international conference on computer vision*, 2017, pp. 2961–2969.
- [31] S. Umeyama, “Least-squares estimation of transformation parameters between two point patterns,” *IEEE Transactions on Pattern Analysis & Machine Intelligence*, vol. 13, no. 04, pp. 376–380, 1991.
- [32] K. He, X. Zhang, S. Ren, and J. Sun, “Deep residual learning for image recognition,” in *Proceedings of the IEEE conference on computer vision and pattern recognition*, 2016, pp. 770–778.
- [33] D. Hendrycks and K. Gimpel, “Gaussian error linear units (gelus),” *arXiv preprint arXiv:1606.08415*, 2016.
- [34] D. Zhang, F. He, Z. Tu, L. Zou, and Y. Chen, “Pointwise geometric and semantic learning network on 3d point clouds,” *Integrated Computer-Aided Engineering*, vol. 27, no. 1, pp. 57–75, 2020.
- [35] M.-H. Guo, J.-X. Cai, Z.-N. Liu, T.-J. Mu, R. R. Martin, and S.-M. Hu, “Pct: Point cloud transformer,” *Computational Visual Media*, vol. 7, no. 2, pp. 187–199, 2021.
- [36] X. Pan, Z. Xia, S. Song, L. E. Li, and G. Huang, “3d object detection with pointformer,” in *Proceedings of the IEEE/CVF Conference on Computer Vision and Pattern Recognition*, 2021, pp. 7463–7472.
- [37] M. A. Fischler and R. C. Bolles, “Random sample consensus: a paradigm for model fitting with applications to image analysis and automated cartography,” *Communications of the ACM*, vol. 24, no. 6, pp. 381–395, 1981.
- [38] A. X. Chang, T. Funkhouser, L. Guibas, P. Hanrahan, Q. Huang, Z. Li, S. Savarese, M. Savva, S. Song, H. Su *et al.*, “Shapenet: An information-rich 3d model repository,” *arXiv preprint arXiv:1512.03012*, 2015.
- [39] A. Paszke, S. Gross, F. Massa, A. Lerer, J. Bradbury, G. Chanan, T. Killeen, Z. Lin, N. Gimelshein, L. Antiga *et al.*, “Pytorch: An imperative style, high-performance deep learning library,” *Advances in neural information processing systems*, vol. 32, pp. 8026–8037, 2019.
- [40] D. P. Kingma and J. Ba, “Adam: A method for stochastic optimization,” *arXiv preprint arXiv:1412.6980*, 2014.
- [41] A. Farhadi and J. Redmon, “Yolov3: An incremental improvement,” in *Computer Vision and Pattern Recognition*, 2018, pp. 1804–02767.